

# Journal of Materials Chemistry A

Materials for energy and sustainability

Accepted Manuscript

This article can be cited before page numbers have been issued, to do this please use: H. Wang, X. Li, W. Yu and X. Li, *J. Mater. Chem. A*, 2026, DOI: 10.1039/D6TA02867E.



This is an Accepted Manuscript, which has been through the Royal Society of Chemistry peer review process and has been accepted for publication.

Accepted Manuscripts are published online shortly after acceptance, before technical editing, formatting and proof reading. Using this free service, authors can make their results available to the community, in citable form, before we publish the edited article. We will replace this Accepted Manuscript with the edited and formatted Advance Article as soon as it is available.

You can find more information about Accepted Manuscripts in the [Information for Authors](#).

Please note that technical editing may introduce minor changes to the text and/or graphics, which may alter content. The journal's standard [Terms & Conditions](#) and the [Ethical guidelines](#) still apply. In no event shall the Royal Society of Chemistry be held responsible for any errors or omissions in this Accepted Manuscript or any consequences arising from the use of any information it contains.

# Photothermal-Stable Flexible Perovskite Solar Cells Enabled by PbI<sub>2</sub> Suppression with Amino-Functionalized Graphene Quantum Dots

Hao Wang, Xiaoran Li, Wei Yu, and Xin Li\*

School of Electronic Science and Engineering, Xiamen University, Xiamen 361005, China

Corresponding Author: \*

Email: lixin01@xmu.edu.cn (Prof. Xin Li)

## Abstract

The upper interface of inverted flexible perovskite solar cells (FPSCs) is prone to degradation under photothermal stress, leading to the formation of lead iodide (PbI<sub>2</sub>) that severely compromises both device efficiency and operational stability. Herein, we propose amino-functionalized graphene quantum dots (A-GQDs) as a versatile upper interface modifier to address this critical challenge. The abundant Lewis base groups on A-GQDs establish strong coordinated bonding with uncoordinated Pb<sup>2+</sup> and form synergistic hydrogen bonding networks with iodide ions and organic cations, enabling effective defect passivation, favorable energy level alignment, and substantial residual stress release. Remarkably, the A-GQDs layer consistently inhibits photothermal-induced PbI<sub>2</sub> generation and effectively blocks ionic migration during device operation. Benefiting from this multifunctional interface engineering, the optimized flexible devices achieve a champion power conversion efficiency (PCE) of 23.11%, along with exceptional stability under continuous photothermal aging, mechanical bending, and damp heat exposure. This work presents a new interfacial



engineering paradigm that synergistically integrates defect passivation, stress relief, and synergistic stabilization for high-performance flexible photovoltaics.

View Article Online  
DOI: 10.1039/D6TA02867E

## 1. Introduction

Flexible perovskite solar cells (FPSCs) have emerged as core candidates for next-generation portable and wearable energy technologies, owing to their exceptional power-to-weight ratio, superior bending durability, and promising roll-to-roll manufacturing compatibility. However, their commercial viability remains constrained by the critical bottleneck of insufficient long-term operational stability<sup>[1-3]</sup>. Compared to rigid substrates, flexible plastic substrates (e.g., PET, PEN) suffer from intrinsic shortcomings including coefficient of thermal expansion mismatch, low thermal conductivity, and high surface roughness. These inherent drawbacks render the perovskite films deposited thereon more susceptible to synergistic degradation under coupled photo-thermal, moisture, oxygen, and mechanical stresses<sup>[4,5]</sup>. Notably, the upper interface between the perovskite active layer and the top electron transport layer represents the most vulnerable region where defect accumulation, ion migration, and stress-induced lattice distortion are most pronounced, ultimately dictating both device efficiency and stability<sup>[6,7]</sup>. Consequently, developing robust upper interface passivation strategies capable of withstanding dynamic stresses is imperative for achieving synergistic enhancement of high performance and reliability in FPSCs.

In inverted (p-i-n) perovskite solar cells, upper interface engineering is primarily directed toward three concurrent objectives: (1) effective chemical and electronic defect passivation, (2) optimization of energy level alignment to facilitate electron extraction, and (3) suppression of interfacial ion migration and phase segregation<sup>[8]</sup>. In recent years, diverse material systems for upper interface passivation have been extensively explored. For instance, organic small-molecule ammonium salts such as propane-1,3-diamine iodide (PDAI<sub>2</sub>)<sup>[9]</sup> and phenethylammonium chloride (PEACl)<sup>[10]</sup> have been widely employed for shallow-level defect passivation through efficient



coordination with undercoordinated  $\text{Pb}^{2+}$  ions, effectively mitigating non-radiative recombination losses and substantially enhancing open-circuit voltage. Functionalized polymers, including 1,3-bis(2-vinylbenzyl)-1H-benzimidazolium chloride (PVBN)<sup>[11]</sup> and dithienylpyrazinediimide-bithiophene imide (TPDI-BTI)<sup>[12]</sup>, serve as physical capping layers that stabilize the perovskite interface while simultaneously improving contact with fullerene-based electron transport layers. Inorganic materials, such as atomic-layer-deposited  $\text{AlO}_x$ <sup>[13]</sup>,  $\text{PbTe}$ <sup>[14]</sup>, and titanium carbide MXene ( $\text{Ti}_3\text{C}_2\text{T}_x$ )<sup>[15]</sup>, benefit from lattice compatibility and favorable energy alignment with perovskites, making them promising candidates for interfacial epitaxial growth layers that enhance charge extraction and improve device environmental tolerance. Collectively, these efforts have established “chemical interfacial modification” and “physical barrier construction” as two fundamental paradigms for elevating upper interface quality.

Despite significant progress, growing concerns have emerged regarding the fundamental inadequacies of existing upper interface passivation strategies when applied to FPSCs. First, most passivating agents, particularly organic small molecules, exhibit static and passive interactions. While effective in passivating pre-existing defects formed during fabrication, the passivation ability is limited under the condition of continuous external stress, especially under permanent photothermal stress<sup>[16,17]</sup>. Second, many materials—such as certain inorganic compounds or rigid polymers—may improve electron transport but suffer from inherent brittleness or thermo-mechanical mismatch with the perovskite lattice, potentially becoming nucleation sites for microcrack formation under bending stress, thereby compromising mechanical reliability. Most critically, the vast majority of strategies neglect to directly intervene in the core degradation pathway of perovskites under photothermal stress, namely the formation and accumulation of lead iodide ( $\text{PbI}_2$ )<sup>[18,19]</sup>.  $\text{PbI}_2$  not only acts as a non-radiative recombination center but also accelerates interfacial delamination and performance decay upon accumulation<sup>[20]</sup>. Therefore, the development of novel upper interface materials that can dynamically accommodate flexible substrate deformation, actively suppress degradation product formation, and simultaneously fulfill multiple passivation functions represents an urgent imperative



for achieving substantive breakthroughs in FPSCs.

View Article Online  
DOI: 10.1039/D6TA02867E

Among various emerging interface materials, graphene quantum dots (GQDs) have demonstrated great potential as ideal interfacial modifiers owing to their abundant surface functional groups, excellent solution processability, and good mechanical flexibility. To date, the application of GQDs in perovskite solar cells (PSCs) has been extensively explored; however, most studies focus on conventional n-i-p structured rigid PSCs (RPSCs), where GQDs are primarily positioned at the electron transport layer/perovskite interface (ETL/PVK) or used as additive in the perovskite bulk. For instance, Xie et al. modified the SnO<sub>2</sub> ETL with GQDs, which enhanced electron extraction and suppressed interfacial recombination, achieving a power conversion efficiency (PCE) of 20.23%<sup>[21]</sup>. Subsequently, Pang et al. modified SnO<sub>2</sub> by GQDs, further increasing the PCE to 21.1%<sup>[22]</sup>. Gao et al. designed imidazole bromide-functionalized GQDs (I-GQDs) for the SnO<sub>2</sub>/PVK interface, reaching a PCE of 22.37%<sup>[23]</sup>. Zhou et al. prepared GQD and SnO<sub>2</sub> nanoparticle composites (G@SnO<sub>2</sub>) as ETLs to RPSCs and FPSCs, achieving PCE of 19.6% and 17.7%, respectively<sup>[24]</sup>. In addition, GQDs have been used as bulk additives in n-i-p PSCs: Hu et al. incorporated F/N-codoped GQDs into carbon-based PSCs (CPSCs) and use it as the post-treatment agent, improved thermal stability but yielded a moderate PCE of 16.37%<sup>[25]</sup>. Chen et al. introduced fluorinated GQDs (FGQDs) into the anti-solvent, and the FGQDs-optimized RPSCs delivered the PCE of 24.12%<sup>[26]</sup>. Yang et al. introduced fluorographene quantum dots (FGQDs) into the bulk perovskite phase, achieving the PCE of 20.4% in FPSCs<sup>[27]</sup>. In contrast, the utilization of GQDs in inverted (p-i-n) PSCs has been rarely reported. Shin et al. employed GQDs as hole transport layer (HTL) to replace poly(3,4-ethylenedioxythiophene):polystyrene sulfonate (PEDOT:PSS)<sup>[28]</sup>. In combination with graphene transparent electrodes, they achieved efficiencies of 15.38% for FPSCs and 17.15% for RPSCs, respectively. Khan et al. employed N-doped GQDs as an interlayer positioned between PVK/ETL to passivate defects and suppress recombination, the resulting RPSCs efficiency remained 17.10%<sup>[29]</sup>. Gan et al. employed graphite-nitrogen doped GQDs (GN-GQDs) as bulk additive,



achieving the PCE of 19.8% for RPSCs<sup>[30]</sup>. Notably, none of the aforementioned studies on GQDs-based interface engineering or bulk doping provides a systematic assessment of device stability, particularly regarding the specific role of GQDs in bolstering long-term operational resilience under coupled photothermal stress, which is a critical bottleneck that must be addressed to enable the practical deployment of PSCs. Furthermore, in the context of inverted FPSCs, there remains considerable scope for further enhancements in both PCE and operational stability through the judicious incorporation of GQDs.

In response to these challenges, this work innovatively proposes and systematically validates a versatile upper interface reinforcement strategy for FPSCs, employing amino functionalized graphene quantum dots (A-GQDs) as an “intelligent” modifier layer positioned between the perovskite and electron transport layer. This design ingeniously integrates the size advantages of zero-dimensional quantum dots with the chemical reactivity of surface amino groups. On one hand, the amino groups, functioning as strong Lewis bases, effectively anchor undercoordinated Pb<sup>2+</sup> and iodide vacancies at the perovskite surface and grain boundaries, achieving excellent static passivation. On the other hand, we discover A-GQDs act as a “healing agent” under continuous photothermal stress, effectively inhibiting the crystallization and aggregation of deleterious lead iodide, thereby fundamentally mitigating interfacial degradation. Through comprehensive electrochemical characterization and microstructural analysis, this work provides compelling evidence that this strategy not only markedly enhances the PCE of flexible devices but also endows them with exceptional stability under maximum power point (MPP) tracking, photothermal aging, and bending cycling tests, substantially outperforming control devices. The detailed comparison of this work with previous GQDs/graphene studies in PSCs is provided in Table S1. This study offers a novel and efficient material pathway toward resolving the long-standing challenge of interfacial dynamic instability in flexible perovskite photovoltaics.



## 2. Results and discussion

View Article Online  
DOI: 10.1039/D6TA02867E

### 2.1 Characterization of A-GQDs

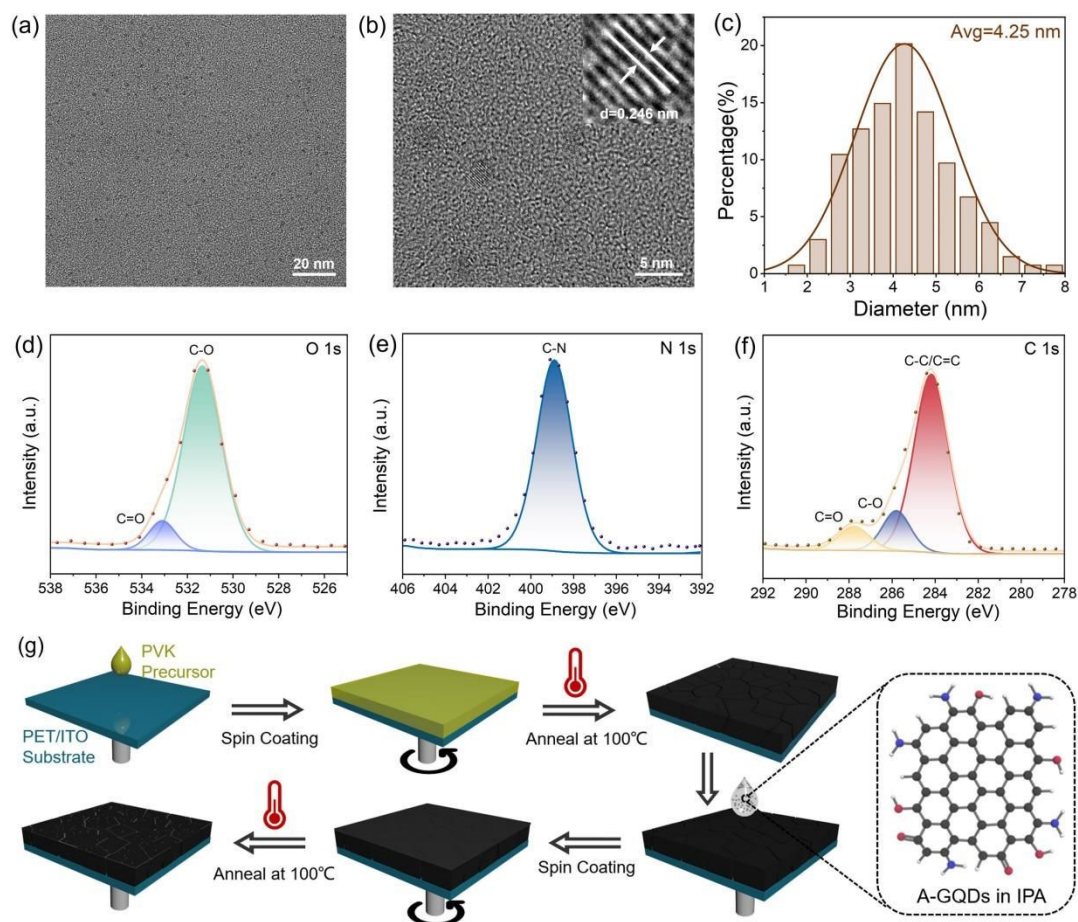


**Figure 1.** (a) TEM image of A-GQDs. (b) High-resolution TEM images of A-GQDs. (c) Particle size distribution diagram of A-GQDs. XPS spectra of (d) C 1s, (e) O 1s and (f) N 1s of A-GQDs. (g) Schematic diagram of preparation process for A-GQDs modified perovskite film.

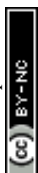
The morphology, structure, chemical composition, and fabrication process of the A-GQDs were systematically characterized to establish their fundamental physicochemical properties as an efficient interface modification material. Figures 1a-c present the morphology and size distribution of A-GQDs. Transmission electron microscopy (TEM) imaging (Figure 1a) clearly reveals that the A-GQDs exhibit excellent monodispersity without noticeable aggregation. High-resolution TEM



(HRTEM, Figure 1b) further resolves the crystalline structure of an individual quantum dot, displaying well-defined lattice fringes with an interplanar spacing of approximately 0.246 nm. Statistical analysis of the A-GQDs size distribution (Figure 1c) yields an average diameter of  $4.25 \pm 0.68$  nm. This uniform nanoscale dimension is critical for forming continuous, pinhole-free ultrathin modification layers on rough flexible perovskite film surfaces, facilitating homogeneous interfacial interactions and efficient charge transport<sup>[31]</sup>.

To gain deeper insight into the surface chemical functionalities of A-GQDs, X-ray photoelectron spectroscopy (XPS) analysis was performed, with results shown in Figures 1d-f. The C 1s spectrum (Figure 1d) can be deconvoluted into three characteristic peaks: the dominant peak at 284.2 eV is assigned to  $sp^2$ -hybridized C-C/C=C bonds, confirming the presence of the graphene  $sp^2$  carbon framework, and peaks at 285.8 eV and 287.7 eV correspond to C-O and C=O bonds, respectively. The O 1s spectrum (Figure 1e) exhibits fitted peaks at 531.3 eV (C=O) and 533.0 eV (C-O), corroborating the C 1s analysis. Most importantly, the N 1s spectrum (Figure 1f) displays a single symmetric peak at 398.9 eV, attributable to C-N bonds, providing direct evidence for the presence of amino ( $-NH_2$ ) functional groups on the graphene quantum dot surface<sup>[32]</sup>. The abundant oxygen- and nitrogen-containing functional groups not only ensure excellent dispersibility of A-GQDs in polar solvents but also furnish active sites for interacting with perovskite components and achieving defect passivation. Fourier-transform infrared (FT-IR) spectroscopy further corroborates the existence of these surface functional groups (Figure S3), while schematic structural representations and simplified models of A-GQDs are presented in Figures S1 and S2, respectively.

As illustrated in Figure 1g, a stable A-GQDs modification layer was formed by directly depositing an A-GQDs solution in isopropanol (IPA) onto the as-prepared perovskite film surface via a one-step spin-coating method, followed by a mild annealing treatment. This fabrication protocol is perfectly compatible with the low-temperature processing requirements of inverted FPSCs, offering significant advantages in terms of cost and manufacturability, and presenting a viable



technological pathway toward large-scale production of high-performance flexible devices.

## 2.2 Interfacial interaction mechanism between A-GQDs and perovskite films

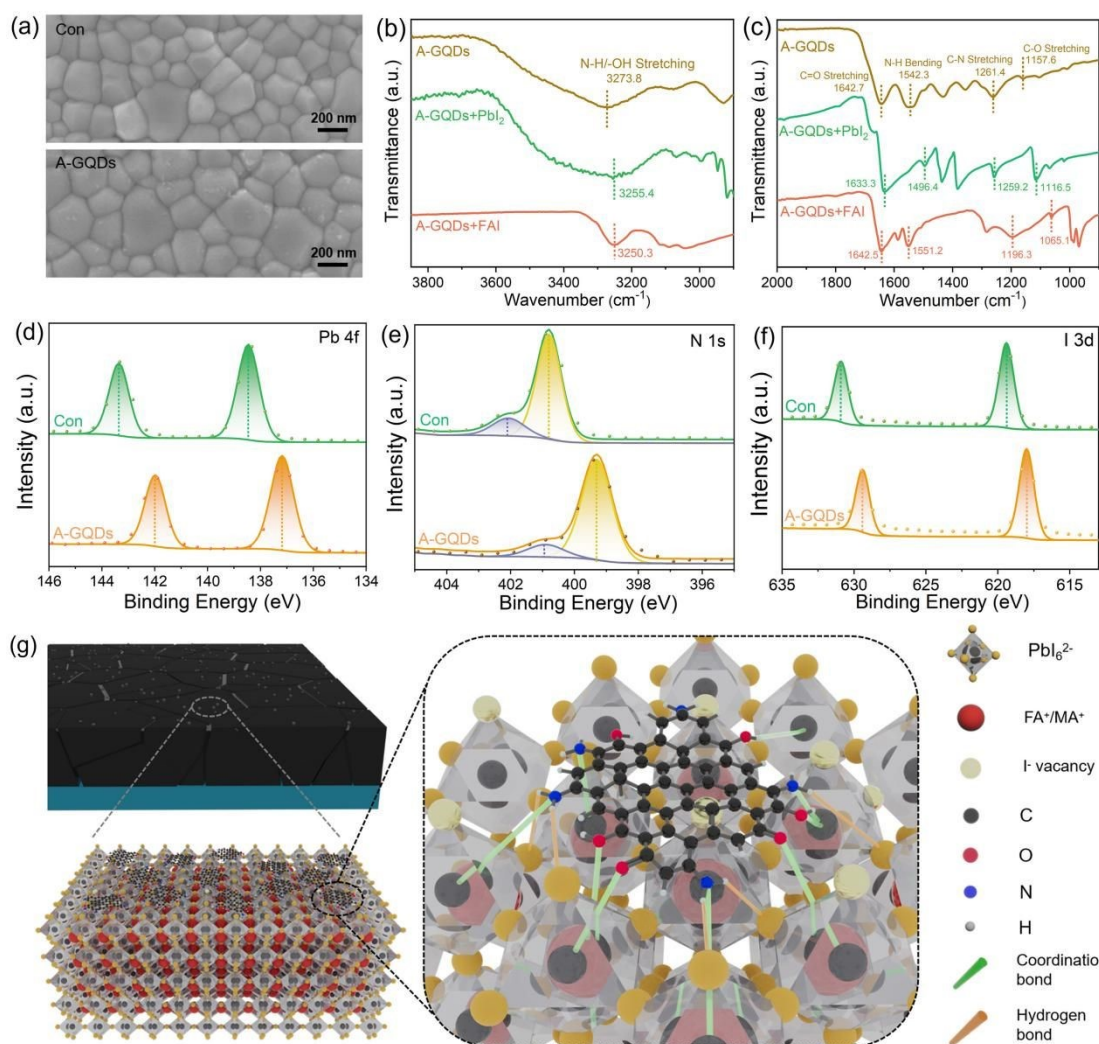


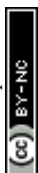
**Figure 2.** (a) SEM images of perovskite films without and with A-GQDs modified. (b), (c) FT-IR spectra of A-GQDs, A-GQDs and PbI<sub>2</sub> mixture, A-GQDs and FAI mixture. XPS spectra of (d) Pb 4f, (e) N 1s and (f) I 3d without and with A-GQDs modified perovskite films. (g) Schematic diagram of interaction mechanism between A-GQDs and perovskite film.

To elucidate the fundamental role of A-GQDs as an interfacial modifier, the



physical and chemical interactions between A-GQDs and the perovskite film are systematically investigated. Figure 2a presents scanning electron microscopy (SEM) images ( $50k\times$  magnification) comparing the surface morphology of pristine (Control) and A-GQDs-modified perovskite films. A uniform coverage of nanoparticles is clearly observed on the modified film surface, providing direct evidence for the successful deposition of the A-GQDs layer. Additional SEM images at  $30k\times$  magnification and corresponding grain size statistics are provided in Figures S4 and S5. Statistical analysis reveals a slight increase in average grain size from 244.92 nm to 276.44 nm upon A-GQDs modification. To understand the origin of the increased grain size after A-GQDs modification, we compared the XRD patterns of control and A-GQDs modified perovskite films (Figure S6). The diffraction intensities of the (001), (002), and (012) planes are all substantially enhanced upon A-GQDs modification, indicating improved crystallinity. Together with the increase of grain size, the XRD evidence suggests that A-GQDs induce secondary grain growth. This phenomenon can be primarily attributed to the Ostwald ripening mechanism, which is well established in perovskite post-treatment studies<sup>[33,34]</sup>. Specifically, the polar IPA solvent and functional groups on A-GQDs, combined with the additional annealing step ( $100\text{ }^{\circ}\text{C}$ ), facilitates the dissolution of smaller, less thermodynamically stable grains and their re-deposition onto larger, more stable grains<sup>[35]</sup>. Collectively, the grain size enlargement arises from the interplay between thermal driving forces and chemical anchoring effects of A-GQDs.

Fourier-transform infrared (FT-IR) spectroscopy was employed to unravel the chemical interaction mechanisms at the molecular level. As shown in Figure 2b and 2c, systematic shifts in characteristic vibrational peaks were observed when A-GQDs were respectively mixed with perovskite precursor components,  $\text{PbI}_2$  and formamidinium iodide (FAI). In the A-GQDs+ $\text{PbI}_2$  system, the pronounced red shifts of the N-H bending ( $-45.9\text{ cm}^{-1}$ ) and C-O stretching ( $-41.1\text{ cm}^{-1}$ ) peaks are characteristic of strong coordination interactions. Specifically, the lone-pair electrons on the amino nitrogen and hydroxyl oxygen atoms are donated to the empty 6p orbitals of  $\text{Pb}^{2+}$ , forming Pb-N and Pb-O bonds<sup>[36]</sup>. The smaller shift of the C-N



stretching ( $-2.2\text{ cm}^{-1}$ ) and C=O stretching ( $-9.4\text{ cm}^{-1}$ ) suggests that while the amino group is involved in coordination, the C-N and C=O bonds are less directly affected. The broad N-H/O-H stretching peak also shifts to lower wavenumber ( $-18.4\text{ cm}^{-1}$ ), further confirming the coordination mechanism. In the A-GQDs+FAI system, hydrogen bonding serves as the dominant interaction. The blue shift of N-H bending ( $+8.9\text{ cm}^{-1}$ ) and red shift of N-H/O-H stretching ( $-23.5\text{ cm}^{-1}$ ) stretching peaks are typical signature of the  $-\text{NH}_2$  group acting as a hydrogen bond donor (N-H...I<sup>-</sup>)<sup>[37]</sup>. The C-O ( $-92.5\text{ cm}^{-1}$ ) and C-N ( $-65.1\text{ cm}^{-1}$ ) stretching exhibit exceptionally large red shift comparing with C=O stretching ( $-0.2\text{ cm}^{-1}$ ), indicating that the carbonyl oxygen and ammonia nitrogen serve as hydrogen bond acceptors (C-O/N...H-N), interacting with the  $-\text{NH}_2^+/-\text{NH}_3^+$  groups of  $\text{FA}^+/\text{MA}^+$ .<sup>[38]</sup> The direct FTIR comparison between pristine and A-GQDs-modified perovskite films further corroborates this interpretation (Figure S7, S8). The shifting peaks of N-H ( $3400.8$  to  $3395.6\text{ cm}^{-1}$ ) and C-N ( $3264.4$  to  $3261.8\text{ cm}^{-1}$ ) stretching vibrations of  $\text{FA}^+/\text{MA}^+$  evidence hydrogen bonding (C-O/N...H-N) between organic cations and A-GQDs. Most importantly, the Pb-I lattice stretching red shifts from  $595.3$  to  $592.1\text{ cm}^{-1}$ , directly demonstrating Lewis-base groups ( $-\text{NH}_2$ ,  $-\text{OH}$  and  $\text{C}=\text{O}$ ) on A-GQDs donate lone-pair electrons to undercoordinated  $\text{Pb}^{2+}$ , forming coordination bonds (Pb-N, Pb-O) that reduce the Pb-I bond order and cause the characteristic red shift<sup>[39]</sup>. Collectively, these results demonstrate that a multimodal bonding configuration-comprising Pb-O/N coordination bonds alongside N-H...I<sup>-</sup> and C-O/N...H-N hydrogen bonds-collectively establishes the chemical foundation for the robust anchoring of A-GQDs onto the perovskite surface.

X-ray photoelectron spectroscopy (XPS) depth profiling provides direct evidence for the aforementioned chemical interactions. As shown in Figure 2d, compared to the pristine perovskite film, the Pb 4f characteristic peaks (Pb 4f 7/2 and Pb 4f 5/2) of A-GQDs-modified films exhibit a pronounced shift toward lower binding energies, from  $138.47\text{ eV}$  and  $143.36\text{ eV}$  to  $137.17\text{ eV}$  and  $142.02\text{ eV}$ , respectively. This decrease in binding energy signifies increased electron density around Pb atoms, directly attributable to successful coordination between electron-rich O/N atoms of

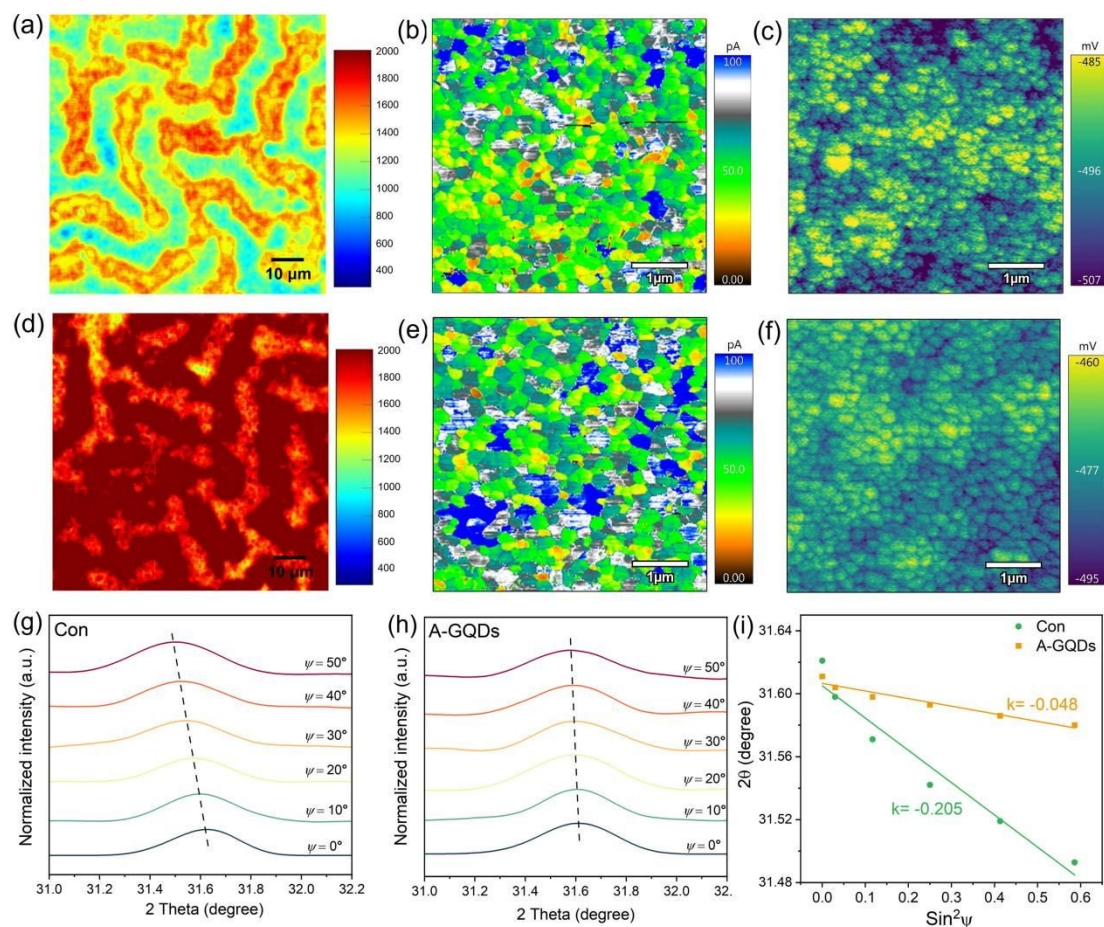


A-GQDs and undercoordinated  $\text{Pb}^{2+}$  defect sites, with electron transfer from A-GQDs to  $\text{Pb}^{40}$ . Similarly, as illustrated in Figure 2e, the N 1s peaks associated with organic cations in the perovskite (corresponding to  $-\text{NH}_2$  and  $-\text{NH}_3^+$  of  $\text{FA}^+/\text{MA}^+$ , respectively) undergo distinct chemical shifts, further supporting the hydrogen bonding interactions between hydroxyl oxygen of A-GQDs and perovskite organic cations<sup>[41]</sup>. Moreover, the I 3d peaks shift from 619.4/630.9 eV to lower binding energies of 617.9/629.4 eV (Figure 2f), consistent with the formation of N-H...I hydrogen bonds and the concomitant suppression of interfacial iodine vacancies<sup>[42]</sup>.

This synergistic passivation effect, wherein “coordination-dominated targeted defect healing” operates in concert with “hydrogen bonding-driven global stabilization”, positions A-GQDs as a “versatile interfacial hub” within the perovskite interface architecture. This dual-modal chemical passivation mechanism, combined with the physical capping effect, collectively constructs an integral, stable, and defect-minimized upper perovskite interface. Based on the comprehensive analysis above, the schematic illustration of the synergistic multifunctional interaction mechanism of A-GQDs at the perovskite interface is proposed, as depicted in Figure 2g.



## 2.3 Synergistic optimization of perovskite film by A-GQDs

View Article Online  
DOI: 10.1039/D6TA02867E

**Figure 3.** PL mapping images of (a) control and (d) A-GQDs modified perovskite films. C-AFM current maps of control (b) and (e) A-GQDs modified perovskite films. KPFM images of (c) control and (f) A-GQDs modified perovskite films. GIXRD patterns with different instrumental diffraction  $\psi$  values (0°–50°) of (g) control and (h) A-GQDs modified perovskite films. (i) The corresponding linear fit of  $2\theta$ - $\sin^2\psi$ .

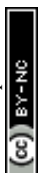
To comprehensively evaluate the impact of A-GQDs interfacial modification on the intrinsic properties of the perovskite active layer, we systematically investigated the optical, electrical, and structural-mechanical characteristics of pristine and modified films. The photophysical properties were first examined following A-GQDs modification. As shown in Figure S9, the modified films exhibit enhanced UV-vis absorption intensity across the 300–800 nm range, suggesting that the A-GQDs layer improves photon harvesting capability<sup>[43]</sup>. Photoluminescence (PL) measurements



reveal effective defect passivation: the A-GQDs-modified films display significantly higher PL peak intensity compared to control films (Figure S10a), directly indicating effective suppression of non-radiative recombination channels. This finding is further corroborated by the PL mapping spatial distributions presented in Figures 3a and 3d, where modified films exhibit stronger and more uniform PL signals, demonstrating that the passivation effect of A-GQDs is macroscopically homogeneous. Time-resolved photoluminescence (TRPL) analysis provides quantitative evidence for carrier dynamics, as shown in Figure S10b. The average carrier lifetime ( $\tau_{ave}$ ) of modified films is substantially prolonged from 286.72 ns to 671.59 ns (Table S2). This extended carrier lifetime unequivocally confirms that A-GQDs effectively reduce trap-assisted non-radiative recombination rates through defect passivation, facilitating the diffusion and collection of photogenerated carriers.

To elucidate the influence of the modification layer on local charge transport behavior and interfacial energy levels, conductive atomic force microscopy (C-AFM) and Kelvin probe force microscopy (KPFM) measurements were performed. C-AFM images (Figure 3b) reveal that the pristine perovskite film exhibits inhomogeneous conductivity distribution with extensive dark regions (low current), corresponding to grain boundaries or areas with high defect density. In contrast, following A-GQDs modification (Figure 3e), the current signal across the film surface is significantly enhanced and uniformly distributed, demonstrating that interfacial modification effectively promotes charge transport and reduces local electrical heterogeneity<sup>[44]</sup>. KPFM measurements of surface contact potential difference (CPD), presented in Figures 3c, 3f, and S11, show that the surface potential of control films is -496 mV, which increases to -477 mV upon A-GQDs modification. This increase in CPD (decrease in absolute value) signifies a reduction in the work function of the film surface. Such energy level modulation is advantageous for lowering the electron extraction barrier between the perovskite and the upper electron transport layer (ETL), thereby enhancing charge separation and transport efficiency in the device<sup>[45]</sup>.

A fundamental requirement for flexible devices is the ability of the active layer to withstand sustained mechanical bending stress. We employed multiple techniques



to assess the improvement in film microstructure and mechanical properties conferred by A-GQDs. Atomic force microscopy (AFM) analysis (Figure S12) reveals that the root mean square (RMS) surface roughness of modified films decreases substantially from 28.32 nm to 19.53 nm, indicating that A-GQDs fill surface voids and create a more planar interface. Furthermore, grazing-incidence X-ray diffraction (GIXRD) combined with the  $2\theta$ - $\sin^2\psi$  method was employed for in-depth analysis of residual film stress (Note S1). The (012) crystallographic plane ( $2\theta \approx 31.6^\circ$ ) was selected for stress analysis (Figures 3g and 3h) due to its high diffraction angle and multiplicity factor, which provide the most reliable structural information<sup>[46]</sup>. Calculation results demonstrate that control films exhibit significant residual tensile stress reaching 48.52 GPa, whereas A-GQDs-modified films show a substantially reduced residual stress of 11.36 GPa (Figure 3i). Additionally, the Young's modulus of A-GQDs-modified films decreases from 10.324 GPa to 5.528 GPa (Figure S13). The A-GQDs layer thus functions as a "stress buffer", releasing strain between the perovskite and subsequent functional layers, thereby significantly enhancing the mechanical durability of flexible devices<sup>[47]</sup>.



## 2.4 A-GQDs modification enables high-efficiency FPSCs

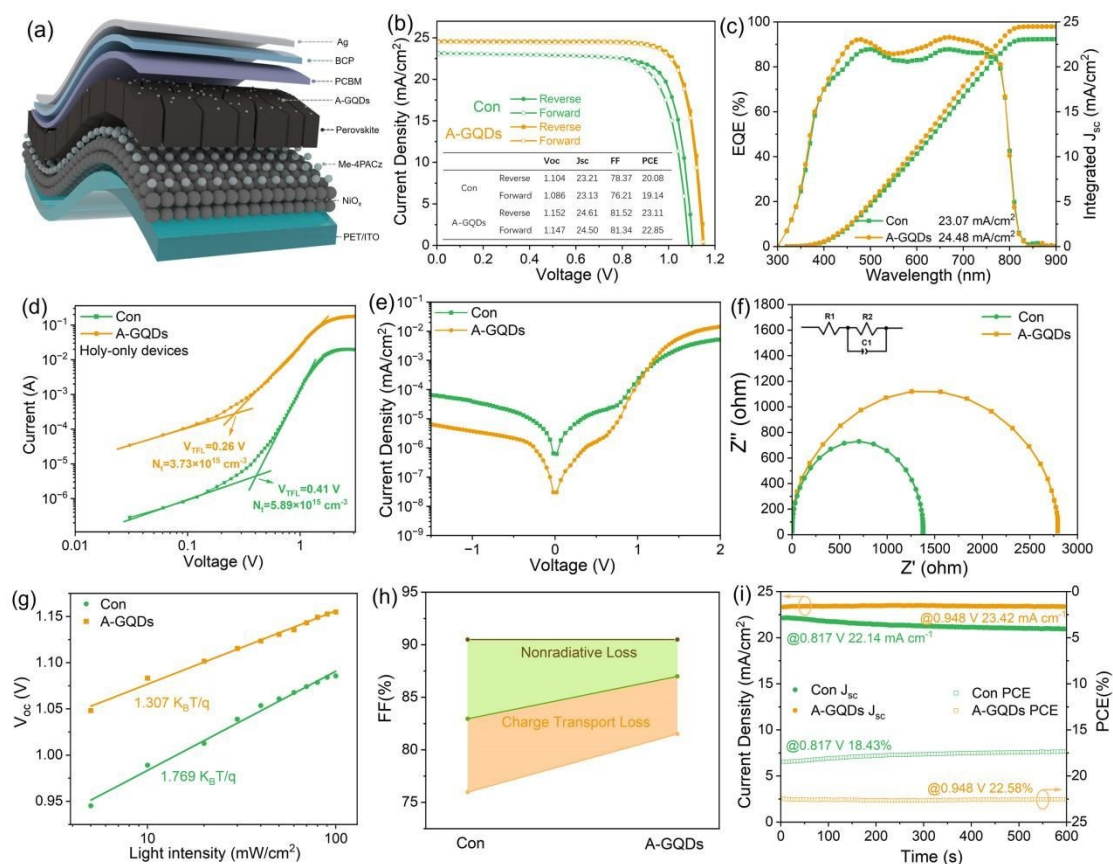


**Figure 4.** (a) Schematic illustration of the FPSCs. (b)  $J$ - $V$  curves of both reverse and forward scans of control and A-GQDs optimized FPSCs. (c) EQE spectra and integrated  $J_{SC}$  curves of control and A-GQDs optimized FPSCs. (d) The holy-only SCLC curves of control and A-GQDs modified FPSCs. (e) Dark  $J$ - $V$  curves of control and A-GQDs modified FPSCs. (f) Nyquist plots of the control and A-GQDs optimized FPSCs. (g) Light intensity dependence of  $V_{oc}$ . (h) FF Shockley-Queisser (S-Q) limit diagram of the device (brown, green and orange spheres correspond to  $FF_{S-Q}$ ,  $FF_{max}$  and measured FF respectively; green areas correspond to non-radiation loss; orange areas correspond to charge transfer loss). (i) Stabilized photocurrent outputs and PCEs, corresponding to the MPP tracking.

Building upon the preceding demonstration that A-GQDs effectively passivate film defects, optimize photophysical properties, and enhance mechanical flexibility, this section integrates the modifier into complete FPSCs to systematically evaluate the



impact of A-GQDs interfacial modification on device photovoltaic performance, charge carrier dynamics, and energy loss mechanisms. Figure 4a presents the schematic illustration of the inverted FPSCs architecture employed in this study, with the specific configuration PET/ITO/NiO<sub>x</sub>/MeO-4PACz/Perovskite/A-GQDs/PCBM/BCP/Ag.

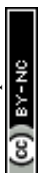
To assess the effect of A-GQDs modification on device performance, control and A-GQDs-optimized devices were fabricated and characterized by current density-voltage ( $J$ - $V$ ) measurements. As shown in Figure 4b, the control device achieves a PCE of 20.08%, with an open-circuit voltage ( $V_{oc}$ ) of 1.104 V, short-circuit current density ( $J_{sc}$ ) of 23.21 mA cm<sup>-2</sup>, and fill factor (FF) of 78.37%, exhibiting pronounced hysteresis. In contrast, the A-GQDs-optimized device attains a champion PCE of 23.11% with substantially reduced hysteresis, accompanied by enhanced photovoltaic parameters:  $V_{oc}$  of 1.152 V,  $J_{sc}$  of 24.61 mA cm<sup>-2</sup>, and FF of 81.52% (Table S3). Systematic optimization of A-GQDs concentration in isopropanol (0, 0.5, 1.0, and 1.5 mg mL<sup>-1</sup>) identifies 1.0 mg mL<sup>-1</sup> as the optimal concentration (Figure S14). To demonstrate the scale-up potential of A-GQDs in FPSCs, we fabricated large-area flexible perovskite solar modules with a substrate size of 5 cm × 5 cm (active areas about 10.45 cm<sup>2</sup>). As shown in Figure S15 and Table S4, the champion A-GQDs-optimized module achieved the PCE of 20.24%, with  $V_{oc}$  of 6.466 V,  $J_{sc}$  of 4.09 mA cm<sup>-2</sup>, and FF of 76.56. In contrast, the control module (without A-GQDs) delivered the PCE of 18.02%. Notably, the A-GQDs modified module exhibited substantially reduced hysteresis between forward and reverse scans, indicating that interface modification effectively suppresses ion migration and charge trapping in large-area perovskite films.

External quantum efficiency (EQE) spectra and corresponding integrated current densities are presented in Figure 4c. The A-GQDs-modified device exhibits enhanced EQE response across the entire spectral range, with particularly pronounced improvement in the 400-750 nm region. The integrated current density increases from 23.07 mA cm<sup>-2</sup> for the control device to 24.48 mA cm<sup>-2</sup> for the optimized device, showing excellent agreement with  $J$ - $V$  measurements. Differentiation of the EQE



spectrum for the optimized device (Figure S16) confirms an optical bandgap of 1.55 eV for the perovskite absorber, consistent with expectations<sup>[48]</sup>. To elucidate the underlying electrical mechanisms responsible for the enhanced photovoltaic performance upon A-GQDs modification, the trap-state density within perovskite films was first evaluated by space-charge-limited current (SCLC) method. Hole-only devices with the structure ITO/NiO<sub>x</sub>/Perovskite/Spiro-OMeTAD/Ag were fabricated and characterized, as shown in Figure 4d. The trap-filled limit voltage ( $V_{TFL}$ ) extracted from the dark  $J$ - $V$  curves was employed to calculate the trap-state density according to Note S2. The control device exhibits a  $V_{TFL}$  of 0.41 V, corresponding to a trap-state density of  $5.89 \times 10^{15} \text{ cm}^{-3}$ , whereas the optimized device displays a reduced  $V_{TFL}$  of 0.26 V, corresponding to a diminished trap-state density of  $3.73 \times 10^{15} \text{ cm}^{-3}$ . Figure 4e presents the dark  $J$ - $V$  characteristics and corresponding Tafel plots for both devices. The optimized device exhibits substantially lower dark current density near zero bias compared to the control, indicating effective suppression of leakage current pathways and enhanced shunt resistance<sup>[49]</sup>. Electrochemical impedance spectroscopy (EIS) measurements (Figure 4f) further corroborate these findings, revealing that the optimized device possesses significantly higher recombination resistance ( $R_{rec}$ ), demonstrating effective suppression of interfacial non-radiative recombination processes and enabling more efficient separation and extraction of photogenerated carriers<sup>[50]</sup>.

To gain deeper insight into the carrier recombination mechanisms within the devices, the dependence of  $V_{oc}$  on light intensity ( $I$ ) was investigated (Figure 4g). According to the relationship of  $V_{oc} \propto (nkT/q) \ln(I)$ , the fitted slope provides information on the dominant recombination kinetics<sup>[51]</sup>. The control device exhibits a slope of 1.769 kT/q, substantially deviating from the ideal value of unity, indicating pronounced trap-assisted Shockley-Read-Hall (SRH) recombination. Remarkably, the optimized device displays a reduced slope of 1.307 kT/q, approaching the ideal value and confirming that A-GQDs modification effectively suppresses trap-dominated SRH recombination. This finding is in excellent agreement with the conclusions drawn from SCLC, EIS, and steady-state/transient PL measurements. Quantitative



analysis of FF losses based on the Shockley-Queisser (S-Q) limit theory is presented in Figure 4h and Note S3. The A-GQDs-optimized device exhibits reduced non-radiative recombination losses and diminished charge transport losses compared to the control, consistent with the observed enhancement in both  $V_{oc}$  and FF.

To further elucidate the origins of  $V_{oc}$  and FF enhancement, ultraviolet photoelectron spectroscopy (UPS) measurements were performed (Figure S17). The calculated work function ( $W_F$ ) of the pristine perovskite film is approximately 5.30 eV, which decreases to 4.84 eV upon A-GQDs modification (Note S4), showing excellent agreement with the increased surface potential (reduced work function) observed in KPFM measurements. Based on these findings, energy level alignment diagrams between the perovskite and PCBM electron transport layer were constructed before and after modification (Figure S18). The relatively high work function of the pristine perovskite results in a substantial energy mismatch between its conduction band minimum and the LUMO level of PCBM, creating an electron extraction barrier. Following A-GQDs modification, the reduced perovskite work function induces an upward shift of the conduction band, transforming the energy level alignment from an unfavorable “cliff-like” configuration to a more desirable “staircase-like” configuration. This optimized alignment substantially reduces the interfacial energy barrier, facilitating efficient electron extraction (Figure S19). Photogenerated electrons can thus transfer more readily from the perovskite conduction band into PCBM, minimizing interfacial accumulation and recombination losses. This energy level optimization mechanism constitutes a fundamental origin of the concurrently enhanced  $V_{oc}$  and FF in A-GQDs-modified devices<sup>[52]</sup>.

Beyond investigating the efficiency enhancement mechanisms conferred by A-GQDs, the operational stability of devices under continuous MPP tracking for 600 s was evaluated (Figure 4i). In contrast to the control device, the A-GQDs-optimized device exhibits superior output stability throughout the testing period. This enhanced operational robustness correlates closely with the defect passivation, interfacial energy level optimization, and residual stress relief demonstrated in preceding sections, collectively confirming that A-GQDs modification substantially improves



the durability of flexible devices under sustained operation.

View Article Online  
DOI: 10.1039/D6TA02867E

## 2.5 Stability enhancement of FPSCs by A-GQDs

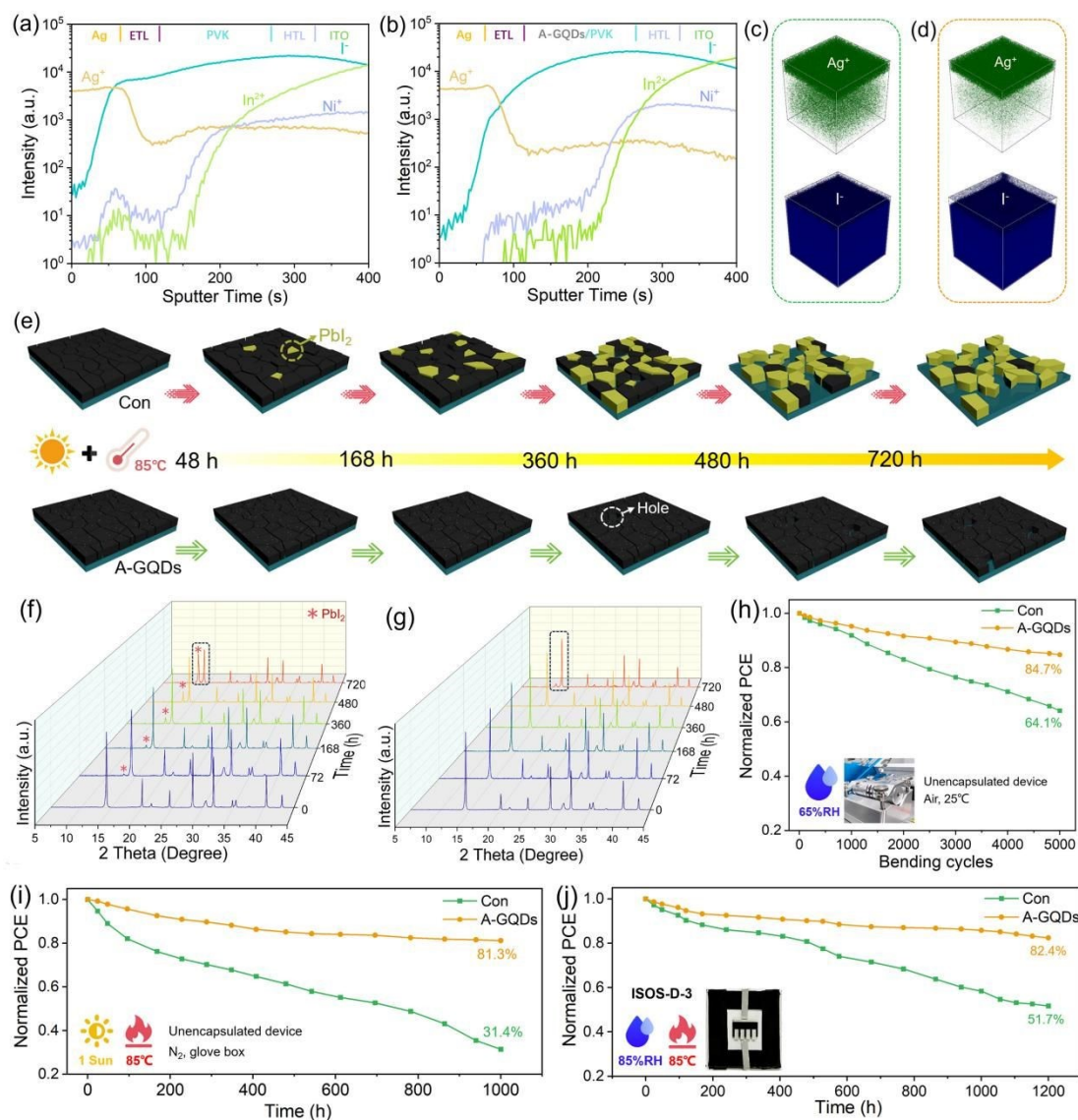


**Figure 5.** Depth profiles of TOF-SIMS for aged (a) control and (b) A-GQDs modified devices, aging at 1-sun illumination and 85 °C heating for 100 hours in N<sub>2</sub>. Volume distribution of Ag<sup>+</sup> and I<sup>-</sup> of (c) control and (d) A-GQDs modified devices. (e) Aging schematic diagram of control perovskite films at different times from 0h to 720h under continuous 1-sun illumination and 85 °C heating corresponding to SEM aging measurement. XRD aging spectrum of (f) control and (g) A-GQDs modified perovskite films under 1-sun illumination and 85 °C heating. (h) The mechanical stability of unencapsulated FPSCs at a 10 mm bending radius in air. (i) Operational



stability of unencapsulated FPSCs under 1-sun illumination and 85 °C heating in N<sub>2</sub>. (j) Stability testing of encapsulated FPSCs in the dark at 85 °C and 85% RH.

View Article Online  
DOI: 10.1039/C9TA02867E

Operational stability remains one of the most critical bottlenecks impeding the practical deployment of FPSCs. This section systematically evaluates the impact of A-GQDs modification on the durability of both perovskite films and complete FPSCs under various aging conditions.

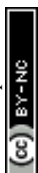
Ion migration, particularly the diffusion of I<sup>-</sup> toward the metal electrode and the reverse infiltration of Ag<sup>+</sup> into the perovskite layer, constitutes a key mechanism underlying the performance degradation of FPSCs. To investigate the inhibitory effect of A-GQDs modification on ion migration, time-of-flight secondary ion mass spectrometry (TOF-SIMS) depth profiling was performed on complete devices after photothermal aging (100 h). In the control device, I<sup>-</sup> ions are distributed not only within the perovskite layer but also exhibit strong signals in the near-surface region adjacent to the Ag electrode, indicating substantial diffusion of I<sup>-</sup> to the device surface. Simultaneously, Ag<sup>+</sup> signals are abundantly present throughout the perovskite depth profile, demonstrating backward diffusion of silver electrode metal ions into the perovskite active layer (Figures 5a and 5c). The A-GQDs-optimized device presents a markedly different distribution profile: I<sup>-</sup> signals are effectively confined within the perovskite layer with significantly reduced intensity at the surface, while the diffusion depth and intensity of Ag<sup>+</sup> into the perovskite layer are substantially suppressed (Figures 5b and 5d). Furthermore, the Ag<sup>+</sup> surface 2D mapping images (Figure S20) reveal that the control device exhibits low-intensity, non-uniform Ag<sup>+</sup> signals on the surface, likely attributable to the formation of AgI clusters via reaction between diffused Ag<sup>+</sup> and I<sup>-</sup>[<sup>53</sup>]. In contrast, the optimized device displays higher intensity and more uniform Ag<sup>+</sup> signals, indicating preservation of the Ag electrode integrity and effective suppression of interfacial reactions. These TOF-SIMS results provide direct evidence that the A-GQDs modification layer functions as a critical “ion diffusion barrier” during device operation. The multimodal chemical bonding network formed between A-GQDs and the perovskite effectively anchors susceptible mobile ions,



thereby significantly enhancing device operational stability.

To intuitively assess the impact of A-GQDs on the photothermal stability of perovskite films, control and A-GQDs-modified films were subjected to accelerated aging under coupled stress conditions comprising 1 sun illumination (AM 1.5G) and 85°C for up to 720 hours, with morphological evolution monitored in situ by SEM. As shown in Figure S21, the control film exhibits localized degradation signatures at the early aging stage (24 h), with the film surface rapidly becoming covered by numerous block-like crystals as aging progresses. Based on XRD results (detailed below), these crystals are identified as lead iodide (PbI<sub>2</sub>), the degradation product. By 720 h, the control film is completely eroded by PbI<sub>2</sub>, with the original perovskite grain morphology becoming virtually unrecognizable. In striking contrast, the A-GQDs-modified film demonstrates exceptional morphological stability throughout the entire aging process (Figure S22). Although a few pinholes gradually emerge on the film surface over time, the grain structure remains intact up to 720 h, with no observable PbI<sub>2</sub> crystal precipitation. This comparison provides compelling evidence that the A-GQDs modification layer effectively suppresses photothermal stress-induced perovskite decomposition. Based on these observations, a schematic mechanism illustrating A-GQDs inhibition of perovskite photothermal degradation is presented in Figure 5e.

X-ray diffraction (XRD) analysis provides quantitative crystallographic evidence corroborating the morphological observations. The evolution of XRD patterns for control and A-GQDs-modified films during photothermal aging are presented in Figures 5f and 5g, respectively. For the control film (Figure 5f), the intensity of the (001) principal diffraction peak progressively attenuates with aging time, while the PbI<sub>2</sub> characteristic peak at 12.8° rapidly intensifies. By 720 h, the PbI<sub>2</sub> peak intensity becomes comparable to that of the perovskite, indicating severe film decomposition. In contrast, although the (001) peak intensity of the A-GQDs-modified film also decreases with aging time, the rate is markedly slower (Figure 5g). The PbI<sub>2</sub> characteristic exhibits only negligible growth throughout the entire aging process, with intensity substantially lower than that of the control film. These results directly



confirm that A-GQDs modification effectively suppresses perovskite lattice decomposition under photothermal stress, retarding  $\text{PbI}_2$  generation and accumulation, thereby ensuring long-term structural stability of the film at its source. Additionally, the influence of A-GQDs modification on the surface hydrophilicity/hydrophobicity of perovskite films was evaluated (Figure S23). A-GQDs modification increases the water contact angle from  $53.30^\circ$  to  $81.74^\circ$ , rendering the surface more hydrophobic. The more hydrophobic surface contributes to prevent ambient moisture from penetrating into the perovskite layer, thereby enhancing the moisture stability of the device.

The operational stability of complete FPSCs devices under various stress conditions was systematically evaluated. Mechanical bending stability, a core requirement for flexible devices, was assessed by subjecting FPSCs to repeated bending at a 10 mm radius under 65% relative humidity (Figure 5h). The control device retains only 64.1% of its initial efficiency after 5000 bending cycles, whereas the A-GQDs-optimized device maintains 84.7% of its original efficiency. This enhanced bending durability correlates closely with the mechanical optimization effects conferred by A-GQDs, including residual stress relief and reduced Young's modulus demonstrated in preceding sections. Photothermal coupling stability, critical for assessing device practicality, was evaluated by tracking device performance under continuous 1 sun illumination combined with  $85^\circ\text{C}$  heating (Figure 5i). The control device exhibits rapid performance decay, retaining only 31.4% of its initial efficiency after 1000 h. Remarkably, the A-GQDs-optimized device demonstrates exceptional photothermal tolerance, maintaining 81.3% of its initial efficiency after 1000 h. This result aligns closely with the ion migration suppression effects revealed by TOF-SIMS and the inhibited  $\text{PbI}_2$  formation evidenced by SEM and XRD, confirming that A-GQDs effectively suppress photothermal-induced degradation reactions. Damp heat stability, simulating extreme environmental conditions that photovoltaic modules may encounter during outdoor operation, was investigated by aging encapsulated devices in a constant temperature-humidity chamber at 85% relative humidity and  $85^\circ\text{C}$  (Figure 5j). The control device undergoes continuous performance degradation,

View Article Online  
DOI: 10.1039/D6TA02867E



retaining only 51.7% of its initial efficiency after 1200 h. In contrast, the optimized device maintains 82.4% of its initial efficiency under identical aging conditions. The synergistic effect of the hydrophobic surface and the barrier against moisture/oxygen ingress substantially delays interface degradation induced by humidity. Furthermore, unencapsulated devices were directly exposed to ambient air at 65% relative humidity for storage stability assessment (Figure S24). The control device retains only 40.2% of its initial efficiency after 1400 h, while the A-GQDs-optimized device exhibits superior storage stability, maintaining 83.6% of its initial efficiency over the same period.

### 3. Conclusions

This study addresses the critical challenge of upper interface instability in FPSCs under photothermal stress, which triggers detrimental  $\text{PbI}_2$  formation and accelerates performance degradation. A-GQDs are innovatively proposed and systematically validated as an effective multifunctional interface modifier. The A-GQDs layer transcends conventional static passivation, exhibiting sustained passivation and stress-buffering capabilities that suppress  $\text{PbI}_2$  accumulation, block ion migration, release residual stress, and enhance mechanical flexibility. A-GQDs-modified F-PSCs achieve 23.11% efficiency with minimal hysteresis, retaining 81.3% of initial performance after 1000 h photothermal aging (versus 31.4% for control), along with superior bending, damp heat, and storage stability. By synergistically enabling defect passivation, energy alignment, ion blocking, degradation suppression, and stress relief, this work provides a novel pathway toward resolving the efficiency-stability dilemma in flexible perovskite photovoltaics.

### Acknowledgement

This work was supported by the National Natural Science Foundation of China (No. 62175204), the National Key R&D Program of China (No. 2022YFE0118400).



## Conflict of Interest

View Article Online  
DOI: 10.1039/D6TA02867E

The authors declare no conflict of interest.

## Reference

- [1] J. Han, K. Park, S. Tan, Y. Vaynzof, J. Xue, E.W.-G. Diau, M.G. Bawendi, J.-W. Lee, I. Jeon, Perovskite solar cells, *Nature Reviews Methods Primers*, 5 (2025) 3.
- [2] H.S. Jung, G.S. Han, N.-G. Park, M.J. Ko, Flexible Perovskite Solar Cells, *Joule*, 3 (2019) 1850–1880.
- [3] H. Wang, X. Li, In-Situ Polymerization Strategies for Flexible Perovskite Solar Cells: Mechanisms and Prospects, *Advanced Materials Technologies*, 10 (2025) 2401606.
- [4] S. Wang, W. Li, C. Yu, W. Shi, Q. Kang, F. Cao, K. Gao, L. Yang, B. Yang, J. Zhou, S. Yang, Q. Wang, Q. Fei, X. Chen, G. Chen, P. Chen, Z. Li, W.-C. Hsu, Z. Yan, Y. Bai, W. Liu, S. De Wolf, X. Yang, X. Zhang, Flexible perovskite/silicon tandem solar cells with 33.6% efficiency, *Nature*, 649 (2026) 59–64.
- [5] Z. Xu, R. Yu, Q. Lv, H. Jia, Q. Guo, T. Xue, R. Wang, H. Gao, E. Zhou, Z.a. Tan, Tensile strain regulation via grain boundary buffering for flexible perovskite solar cells, *Nature Communications*, 17 (2025) 322.
- [6] Y. Li, Y. Wang, Z. Xu, B. Peng, X. Li, Key Roles of Interfaces in Inverted Metal-Halide Perovskite Solar Cells, *ACS Nano*, 18 (2024) 10688–10725.
- [7] X. Zhang, S. Wu, H. Zhang, A.K.Y. Jen, Y. Zhan, J. Chu, Advances in inverted perovskite solar cells, *Nature Photonics*, 18 (2024) 1243–1253.
- [8] H. Wang, C. Liu, R. Xu, Y. Zhang, S. De Wolf, K. Wang, Upper Interface Engineering Between Perovskite and Electron Transport Layer Toward Efficient and Stable Inverted Perovskite Solar Cells, *Advanced Materials*, 38 (2026) e13633.
- [9] J. Wang, Y. Wu, J. Zhao, S. Lu, J. Lu, J. Sun, S. Wu, X. Zheng, X. Zheng, X. Tang, M. Ma, S. Yue, K. Liu, Z. Wang, S. Qu, Unraveling the Molecular Size Effect



- on Surface Engineering of Perovskite Solar Cells, *Small Methods*, 8 (2024) 2400043.
- [10] X. Huo, S. Mariotti, Y. Li, T. Guo, C. Ding, P. Ji, S. Yuan, T. Li, N. Meng, X. Liu, J. Zhang, I.N. Rabehi, Y. Zhang, S. Zhao, H. Wang, D. Song, L.K. Ono, Z. Xu, Y. Qi, Unraveling the relationship between the phenethylammonium-induced 2D phase on the perovskite surface and inverted wide bandgap perovskite solar cell performance, *Energy & Environmental Science*, 17 (2024) 8658–8669.
- [11] Z. Dai, Y. Yang, X. Huang, S. Wan, L. Yuan, H. Wei, S. Nie, Z. Liu, Y. Wu, R. Chen, H. Wang, Interfacial crosslinking benzimidazolium enables eco-friendly inverted perovskite solar cells and modules, *Nano Energy*, 131 (2024) 110190.
- [12] Z. Xing, S. Ma, B.-W. Chen, M. An, A. Fan, X. Hu, Y. Wang, L.-L. Deng, Q. Huang, H. Kanda, F.G. Al-Amri, G. Pozzi, Y. Zhang, J. Xia, J. Wu, X. Guo, M.K. Nazeeruddin, Solubilizing and stabilizing C60 with n-type polymer enables efficient inverted perovskite solar cells, *Joule*, 9 (2025) 101817.
- [13] K. Artuk, D. Turkey, M.D. Mensi, J.A. Steele, D.A. Jacobs, M. Othman, X. Yu Chin, S.-J. Moon, A.N. Tiwari, A. Hessler-Wyser, Q. Jeangros, C. Ballif, C.M. Wolff, A Universal Perovskite/C60 Interface Modification via Atomic Layer Deposited Aluminum Oxide for Perovskite Solar Cells and Perovskite–Silicon Tandems, *Advanced Materials*, 36 (2024) 2311745.
- [14] Y.-h. Li, X.-x. Feng, M.-q. Long, M.-q. Cai, J.-l. Yang, B. Liu, Interface engineering of FAPbI<sub>3</sub> for passivating defects and improving stability with lead chalcogenides, *Journal of Central South University*, 31 (2024) 4625–4637.
- [15] V.S.N. Chava, P.S. Chandrasekhar, A. Gomez, L. Echegoyen, S.T. Sreenivasan, MXene-Based Tailoring of Carrier Dynamics, Defect Passivation, and Interfacial Band Alignment for Efficient Planar p–i–n Perovskite Solar Cells, *ACS Applied Energy Materials*, 4 (2021) 12137–12148.
- [16] J. Xing, C. Liu, Q. Cao, F. Xie, X. Zeng, X. Zhang, H. Liu, Molecular-Perspective Insights into Top Interface Passivation in Inverted Perovskite Solar Cells, *Small*, 21 (2025) e06495.
- [17] N. Ahn, M. Choi, Towards Long-Term Stable Perovskite Solar Cells: Degradation Mechanisms and Stabilization Techniques, *Advanced Science*, 11 (2024)



2306110.

View Article Online  
DOI: 10.1039/D6TA02867E

[18] J. Wei, Q. Wang, J. Huo, F. Gao, Z. Gan, Q. Zhao, H. Li, Mechanisms and Suppression of Photoinduced Degradation in Perovskite Solar Cells, *Advanced Energy Materials*, 11 (2021) 2002326.

[19] Z. Wang, Z. Zhang, L. Xie, S. Wang, C. Yang, C. Fang, F. Hao, Recent Advances and Perspectives of Photostability for Halide Perovskite Solar Cells, *Advanced Optical Materials*, 10 (2022) 2101822.

[20] H. Wang, Q. Li, Y. Zhu, X. Sui, X. Fan, M. Lin, Y. Shi, Y. Zheng, H. Yuan, Y. Zhou, H. Jin, H.G. Yang, Y. Hou, S. Yang, Photomechanically accelerated degradation of perovskite solar cells, *Energy & Environmental Science*, 18 (2025) 2254–2263.

[21] J. Xie, K. Huang, X. Yu, Z. Yang, K. Xiao, Y. Qiang, X. Zhu, L. Xu, P. Wang, C. Cui, D. Yang, Enhanced Electronic Properties of SnO<sub>2</sub> via Electron Transfer from Graphene Quantum Dots for Efficient Perovskite Solar Cells, *ACS Nano*, 11 (2017) 9176-9182.

[22] S. Pang, C. Zhang, H. Zhang, H. Dong, D. Chen, W. Zhu, H. Xi, J. Chang, Z. Lin, J. Zhang, Y. Hao, Boosting performance of perovskite solar cells with Graphene quantum dots decorated SnO<sub>2</sub> electron transport layers, *Applied Surface Science*, 507 (2020) 145099.

[23] Z.-W. Gao, Y. Wang, H. Liu, J. Sun, J. Kim, Y. Li, B. Xu, W.C.H. Choy, Tailoring the Interface in FAPbI<sub>3</sub> Planar Perovskite Solar Cells by Imidazole-Graphene- Quantum-Dots, *Advanced Functional Materials*, 31 (2021) 2101438.

[24] Y. Zhou, S. Yang, X. Yin, J. Han, M. Tai, X. Zhao, H. Chen, Y. Gu, N. Wang, H. Lin, Enhancing electron transport via graphene quantum dot/SnO<sub>2</sub> composites for efficient and durable flexible perovskite photovoltaics, *Journal of Materials Chemistry A*, 7 (2019) 1878-1888.

[25] Q. Hu, K. Zhao, M. Liu, S. Riaz, Y. Qi, P. Wei, J. Cheng, Y. Xie, A dual passivation strategy based on F/N co-doped coal-based graphene quantum dots for high-efficiency carbon-based perovskite solar cells, *Journal of Materials Chemistry A*,



12 (2024) 5980-5989.

[26] Y. Chen, J. Chen, X. Wang, P. Deng, Y. Shen, X. Wang, Fluorinated graphene quantum dots-induced defect passivation of perovskite film toward stable and efficient perovskite solar cell, *International Journal of Hydrogen Energy*, 137 (2025) 107-113.

[27] L. Yang, Y. Li, L. Wang, Y. Pei, Z. Wang, Y. Zhang, H. Lin, X. Li, Exfoliated Fluorographene Quantum Dots as Outstanding Passivants for Improved Flexible Perovskite Solar Cells, *ACS Applied Materials & Interfaces*, 12 (2020) 22992-23001.

[28] S.H. Shin, D.H. Shin, S.-H. Choi, Enhancement of Stability of Inverted Flexible Perovskite Solar Cells by Employing Graphene-Quantum-Dots Hole Transport Layer and Graphene Transparent Electrode Codoped with Gold Nanoparticles and Bis(trifluoromethanesulfonyl)amide, *ACS Sustainable Chemistry & Engineering*, 7 (2019) 13178-13185.

[29] F. Khan, M.T. Khan, S. Rehman, F. Al-Sulaiman, Analysis of electrical parameters of p-i-n perovskites solar cells during passivation via N-doped graphene quantum dots, *Surfaces and Interfaces*, 31 (2022) 102066.

[30] X. Gan, S. Yang, J. Zhang, G. Wang, P. He, H. Sun, H. Yuan, L. Yu, G. Ding, Y. Zhu, Graphite-N Doped Graphene Quantum Dots as Semiconductor Additive in Perovskite Solar Cells, *ACS Applied Materials & Interfaces*, 11 (2019) 37796-37803.

[31] Z.-W. Gao, Y. Wang, H. Liu, J. Sun, J. Kim, Y. Li, B. Xu, W.C.H. Choy, Tailoring the Interface in FAPbI<sub>3</sub> Planar Perovskite Solar Cells by Imidazole-Graphene-Quantum-Dots, *Advanced Functional Materials*, 31 (2021) 2101438.

[32] C. Ren, C. Tian, W. Cao, M. Zhang, T. Zhang, J. Tang, F. Zhang, G. Chen, J. Tang, Controllable functionalization of amino-functionalized graphene quantum dots as fluorescent probe for detection of Cu(II) ions detection, *Materials Letters*, 364 (2024) 136393.

[33] N.D. Pham, V.T. Tiong, D. Yao, W. Martens, A. Guerrero, J. Bisquert, H. Wang, Guanidinium thiocyanate selective Ostwald ripening induced large grain for high performance perovskite solar cells, *Nano Energy*, 41 (2017) 476-487.



- [34] Z. Liu, C. Zhu, H. Luo, W. Kong, X. Luo, J. Wu, C. Ding, Y. Chen, Y. Wang, J. Wen, Y. Gao, H. Tan, Grain Regrowth and Bifacial Passivation for High-Efficiency Wide-Bandgap Perovskite Solar Cells, *Advanced Energy Materials*, 13 (2023) 2203230.
- [35] M. Yang, T. Zhang, P. Schulz, Z. Li, G. Li, D.H. Kim, N. Guo, J.J. Berry, K. Zhu, Y. Zhao, Facile fabrication of large-grain  $\text{CH}_3\text{NH}_3\text{PbI}_{3-x}\text{Br}_x$  films for high-efficiency solar cells via  $\text{CH}_3\text{NH}_3\text{Br}$ -selective Ostwald ripening, *Nature Communications*, 7 (2016) 12305.
- [36] X. Chen, L. Ai, H. Ji, W. Song, Silane Doping for Efficient Flexible Perovskite Solar Cells with Improved Defect Passivation and Device Stability, *ACS Applied Materials & Interfaces*, 16 (2024) 23668-23676.
- [37] L. Lin, T.W. Jones, T.C.-J. Yang, X. Li, C. Wu, Z. Xiao, H. Li, J. Li, J. Qian, L. Lin, J.Q. Shi, S.D. Stranks, G.J. Wilson, X. Wang, Hydrogen bonding in perovskite solar cells, *Matter*, 7 (2024) 38-58.
- [38] B. Zhang, M. Li, L. Li, W. Zhang, Y. Song, Z. Wang, Multifunctional Interfacial Passivation via Cooperative Coordination and Hydrogen Bonding for Highly Efficient and Stable Inverted Perovskite Solar Cells, *Advanced Functional Materials*, n/a (2026) e75040.
- [39] J. Nishida, J.P. Breen, K.P. Lindquist, D. Umeyama, H.I. Karunadasa, M.D. Fayer, Dynamically Disordered Lattice in a Layered Pb-I-SCN Perovskite Thin Film Probed by Two-Dimensional Infrared Spectroscopy, *Journal of the American Chemical Society*, 140 (2018) 9882-9890.
- [40] J. Wang, X.-Y. Dai, L. Bi, J. Sun, M. Liu, X. Ji, F.R. Lin, Q. Fu, A.K.Y. Jen, Synergistic iodine and lead chelation with redox cycling via supramolecular engineering for stable and sustainable perovskite solar cells, *Joule*, 9 (2025) 102105.
- [41] X. Feng, M. Tan, M. Li, H. Wei, B. Yang, Polyhydroxy Ester Stabilized Perovskite for Low Noise and Large Linear Dynamic Range of Self-Powered Photodetectors, *Nano Letters*, 21 (2021) 1500–1507.
- [42] S. Xiong, F. Tian, F. Wang, A. Cao, Z. Chen, S. Jiang, D. Li, B. Xu, H. Wu, Y. Zhang, H. Qiao, Z. Ma, J. Tang, H. Zhu, Y. Yao, X. Liu, L. Zhang, Z. Sun, M.



Fahlman, J. Chu, F. Gao, Q. Bao, Reducing nonradiative recombination for highly efficient inverted perovskite solar cells via a synergistic bimolecular interface, *Nature Communications*, 15 (2024) 5607.

[43] J. Yang, J. Wang, Y. Xie, H. Xu, M. Duan, T. Li, J. Wen, C. Zhang, Y. Xia, H. Zhang, Y. Chen, Environmentally Friendly Flexible Perovskite Solar Cells with Promoted Thermal Diffusivity and Suppressed Lead Leakage, *Advanced Energy Materials*, 15 (2025) e01673.

[44] X. Chang, Y. Liu, Y. Ping, N. Wu, T. Yang, C. Tian, Z. Ling, B. Vishal, A.R. Pininti, J.B. Park, S.Y. Jeong, Y. Qin, W.T. Hui, F.S.Y. Yeung, Y.-Y. Yang, H. Liao, A. Prasetio, F.H. Isikgor, M. He, D.S. Utomo, R. Wang, K. Zhao, M. Lanza, H.Y. Woo, M. Heeney, S. De Wolf, Y.-H. Lin, L. Tsetseris, R. Azmi, T.D. Anthopoulos, Multivalent ligands regulate dimensional engineering for inverted perovskite solar modules, *Science*, 391 (2026) 153–159.

[45] Z. Lan, H. Huang, Y. Lu, S. Qu, M. Wang, S. Du, Y. Yang, C. Sun, Q. Zhang, Y. Suo, X. Wang, L. Yan, P. Cui, Z. Zhao, M. Li, Homogenizing the Electron Extraction via Eliminating Low-Conductive Contacts Enables Efficient Perovskite Solar Cells with Reduced Up-Scaling Losses, *Advanced Functional Materials*, 34 (2024) 2316591.

[46] Z. Zheng, F. Li, J. Gong, Y. Ma, J. Gu, X. Liu, S. Chen, M. Liu, Pre-Buried Additive for Cross-Layer Modification in Flexible Perovskite Solar Cells with Efficiency Exceeding 22%, *Advanced Materials*, 34 (2022) 2109879.

[47] S. Tu, Y. Gang, Y. Lin, X. Liu, Y. Zhong, D. Yu, X. Li, Triple Cross-Linking Engineering Strategies for Efficient and Stable Inverted Flexible Perovskite Solar Cells, *Small*, 20 (2024) 2310868.

[48] S. Tu, W. Chen, Y. Gang, Q. Xiong, X. Li, Engineering a thermally robust hole-selective layer for stable flexible perovskite solar cells, *Chemical Engineering Journal*, 503 (2025) 158389.

[49] P. Liao, X. Zhao, G. Li, Y. Shen, M. Wang, A New Method for Fitting Current–Voltage Curves of Planar Heterojunction Perovskite Solar Cells, *Nano-Micro Letters*, 10 (2017) 5.



- [50] B. Roose, K. Dey, M.R. Fitzsimmons, Y.-H. Chiang, P.J. Cameron, S.D. Stranks, Electrochemical Impedance Spectroscopy of All-Perovskite Tandem Solar Cells, *ACS Energy Letters*, 9 (2024) 442–453.
- [51] H. Zhao, J. Ding, X. Liu, D. He, Y. Yu, J. Yi, C. Chen, J. Hou, J. Chen, Intermolecular Interaction Induced Synergistic Uniform Passivation of Grain Boundary Multiple Defects Enables High-Performance Inverted Perovskite Solar Cells, *Advanced Functional Materials*, n/a (2025) 2504424.
- [52] Z. Li, X. Sun, X. Zheng, B. Li, D. Gao, S. Zhang, X. Wu, S. Li, J. Gong, J.M. Luther, Z.a. Li, Z. Zhu, Stabilized hole-selective layer for high-performance inverted p-i-n perovskite solar cells, *Science*, 382 (2023) 284–289.
- [53] X. Lin, Y. Wang, H. Su, Z. Qin, Z. Zhang, M. Chen, M. Yang, Y. Zhao, X. Liu, X. Shen, L. Han, An In-Situ Formed Tunneling Layer Enriches the Options of Anode for Efficient and Stable Regular Perovskite Solar Cells, *Nano-Micro Letters*, 15 (2022) 10.



**Data Availability Statement**View Article Online  
DOI: 10.1039/D6TA02867E

The data that support the findings of this study are available from the corresponding author upon reasonable request.

